Check for updates

Received: 7 March 2024 | Revised: 7 August 2024 | Accepted: 12 August 2024

DOI: 10.1002/elps.202400051

ELECTROPHORESIS

RESEARCH ARTICLE

Electrokinetic particle trapping in microfluidic wells using conductive nanofiber mats

J. Hunter West | **Tonoy K. Mondal** | **Stuart J. Williams**

Department of Mechanical Engineering, University of Louisville, Louisville, Kentucky, USA

Correspondence
Stuart J. Williams, Department of Mechanical Engineering, University of Louisville, Louisville, KY 40208, USA.
Email: stuart.williams@louisville.edu

Funding information
National Science Foundation, Grant/Award Number: 2121008

Abstract

The frequency dependence of electrokinetic particle trapping using large-area (>mm^2) conductive carbon nanofiber (CNF) mat electrodes is investigated. The fibers provide nanoscale geometric features for the generation of high electric field gradients, which is necessary for particle trapping via dielectrophoresis (DEP). A device was fabricated with an array of microfluidic wells for repeated experiments; each well included a CNF mat electrode opposing an aluminum electrode. Fluorescent microspheres (1 μm) were trapped at various electric field frequencies between 30 kHz and 1 MHz. Digital images of each well were analyzed to quantify particle trapping. DEP trapping by the CNF mats was greater at all tested frequencies than that of the control of no applied field, and the greatest trapping was observed at a frequency of 600 kHz, where electrothermal flow is more significantly weakened than DEP. Theoretical analysis and measured impedance spectra indicate that this result was due to a combination of the frequency dependence of DEP and capacitive behavior of the well-based device.

KEYWORDS
dielectrophoresis, electrohydrodynamics, electrokinetics, microparticles, nanofibers

1 | INTRODUCTION

Dielectrophoresis (DEP) is an electrokinetic technique frequently utilized for trapping, sorting, and characterizing both biological [1, 2] and non-biological [3] particles at the micro- and nanoscale. The DEP force is induced when polarizable particles are exposed to high spatial electric field gradients [4]. These high-field gradients are often created using electrodes with sharp geometries (e.g., electrokinetic nanoprobes [5], nanogap electrodes [6], castellated planar electrodes [7], and micro- and nanopores [8–10]). DEP systems with nanoscale electrode geometries often require specialized and expensive microfabrication techniques such as electron beam lithography [11] or plasma-enhanced chemical vapor deposition [12]. Furthermore, specialized nanoscale electrode fabrication, in general, is not amenable to large surface area features with consistent high spatial field gradients throughout. As a result, most DEP systems suffer from limited throughput capability (nL/min) [3, 13]. This limitation is made worse for smaller particle sizes, as the DEP force scales with particle volume. One of the techniques developed to address the throughput limitation is the use of 3D porous media to create insulative DEP trapping systems [14, 15]. Despite the improvements of throughput for microparticle trapping (mL/min), the field gradients necessary to efficiently trap nanoparticles at such flowrates cannot be generated feasibly by these porous media systems because the smallest features are typically on the microscale. To achieve high-throughput trapping of nanoparticles, having the ability to create a large number of conductive nanoscale features

Abbreviations: CNF, carbon nanofibers; DSA, double-sided adhesive; EHD, electrohydrodynamics; ITO, indium tin oxide.

 © 2024 Wiley-VCH GmbH.

(without the need to utilize sophisticated and expensive fabrication techniques) would be beneficial.

Our previous work demonstrated a method to fabricate macroscale (>cm^2) mats of conductive carbon nanofibers (CNF) using electrospinning (an inexpensive process for fiber creation that does not require cleanroom access); the fiber mats were used as electrodes for DEP trapping of particles as small as 20 nm [16]. Those experiments demonstrated the frequency dependence of both DEP and other electrohydrodynamic (EHD) effects, but quantifying particle trapping as a function of frequency and voltage was not conducted. Furthermore, the impact of EHD phenomena such as electrothermal (ET) flow and AC electroosmosis (ACEO) on particle trapping was not studied. In order to use the CNF mats for high-throughput DEP systems, these effects must first be understood. For this study, a microfluidic well device was fabricated without using traditional micro/nanofabrication techniques that incorporated a CNF mat as an electrode. The purpose of this study was to conduct repeatable particle trapping trials across a broad range of electric field frequencies. The frequency dependence of particle trapping performance gave insight into the relative benefit and detriment of these EHD phenomena.

2 | THEORY

2.1 | Dielectrophoresis

DEP is an electrokinetic phenomenon in which a dipole is induced on a neutrally charged polarizable particle when subjected to a nonuniform electric field [17]. The asymmetrical field effect on this dipole results in a net force either toward (positive DEP) or away from (negative DEP) the increasing field strength depending on the dielectric properties of both the particle and the fluid medium. The direction and frequency dependence of the DEP force are determined by the Clausius–Mossotti factor, which can be calculated using the following equation [4]:

$$CM(\omega) = \frac{\tilde{\varepsilon}_p - \tilde{\varepsilon}_m}{\tilde{\varepsilon}_p + 2\tilde{\varepsilon}_m}, \quad \text{where} \quad \tilde{\varepsilon} = \varepsilon - j\frac{\sigma}{\omega} \tag{1}$$

where $\tilde{\varepsilon}$ is the complex permittivity of the particle (subscript p) and fluid medium (subscript m), ε is absolute permittivity, σ is electrical conductivity, ω is angular frequency ($\omega = 2\pi f$), and j is $\sqrt{-1}$. As particle diameter decreases to approach the thickness of the electric double layer, the effect of ion mobility in the double layer introduces a surface conductance K_s that can exceed bulk conductivity σ_{bulk}. Therefore, the total conductivity of a spherical particle can be calculated as the sum of bulk and surface conductivities using [4]

$$\sigma_p = \sigma_{bulk} + \frac{2K_s}{a} \tag{2}$$

where a is particle diameter. Assuming particle homogeneity, the time-averaged magnitude of the DEP force can be calculated by [4]

$$F_{DEP} = 2\pi\varepsilon_m a^3 \mathrm{Re}\,[CM]\,\nabla|E|^2 \tag{3}$$

where Re$[CM]$ is the real component of the Clausius–Mossotti factor. It can be seen from (3) that the DEP force is proportional to particle volume, and therefore the trapping force decays rapidly as particle size is reduced. It can also be seen that the DEP force can be increased through high electric field gradients.

2.2 | Electrohydrodynamics

During previous experiments [16] and those described herein, vortical EHD flow was observed. It was previously assumed that these effects augmented DEP trapping, but further experimental and numerical investigation is required to understand how the combination of EHD phenomena affects trapping. Understanding such effects was part of the motivation of this study. Specifically, ET hydrodynamics and ACEO are of concern.

Joule heating within the fluid medium will cause a temperature gradient and, subsequently, gradients in ε and σ that result in an electrical body force that induces fluid motion [18]. The maximum ET flow velocity depends on field voltage and fluid properties as given by [18]

$$v_{ET,\max} \propto M\frac{\varepsilon_m \sigma_m V^4}{k_m \eta_m} \tag{4}$$

where V is field voltage, k_m is fluid thermal conductivity, and η_m is fluid dynamic viscosity. In Equation (4), M is a dimensionless factor that is a function of temperature T as well as σ, ε, $\frac{\partial\sigma}{\partial T}$, $\frac{\partial\varepsilon}{\partial T}$, and ω [18]. The frequency-dependence of ET flow magnitude comes from this term, which accounts for the transition between the dominance of conductivity and permittivity. From Equation (4) and the expression for M, a relaxation frequency can be calculated at which the ET flow is negligible. For the experiments described herein, the ET flow decays as frequency increases.

ACEO is an EHD phenomenon by which the progressive screening of the electric double layer of an electrode supplying an AC electric field results in an induced fluid motion in the direction of the tangential component of

15222683, 0, Downloaded from https://analyticalsciencejournals.onlinelibrary.wiley.com/doi/10.1002/elps.202400051 by University Of Louisville, Wiley Online Library on [11/11/2024]. See the Terms and Conditions (https://onlinelibrary.wiley.com/terms-and-conditions) on Wiley Online Library for rules of use; OA articles are governed by the applicable Creative Commons License

the electric field [19]. This phenomenon also shows frequency dependence. At low AC frequencies, the surface charge that accumulates on the electrode screens the electric potential, and at high frequencies, insufficient time is for a surface charge to accumulate before reversal of polarity [18]. As such, for a system utilizing ACEO, there exists a frequency of maximum effect above or below which the flow velocity decays; this maximum frequency is typically on the order of 100s of Hz or low kHz [20, 21]. There are several resources available that provide a more in-depth discussion of *ET* flow and ACEO [18, 19, 22].

3 | MATERIALS AND METHODS

3.1 | Microfluidic well device

3.1.1 | Electrospun carbon nanofibers

Mats of electrically CNFs were fabricated using an electrospinning process as described in previous work where their use as electrodes for AC-dielectrophoretic nanoparticle trapping was demonstrated [16]. In brief, a dimethylformamide solution of polyacrylonitrile was doped with carbon nanotubes to increase electrical conductivity and phthalic acid to improve mechanical properties. The solution was electrospun to produce a nanofiber mat, which was subsequently pyrolyzed in an inert atmosphere to carbonize the fibers. Two CNF mats created through this process were used for the study described herein. The mats were ~80 μm in thickness with electrical conductivity measured at 2.55 S/cm, and the fibers' diameters were measured at 267 ± 94 nm [16]. Round disks of the CNF mats 4 mm in diameter were punched from the bulk mat for the fabrication of a well-based testing device. A scanning electron microscopy image of the conductive nanofibers is shown in Figure 1.

3.1.2 | Device assembly

The well-based devices used to characterize the CNF mats' electrokinetic behavior were fabricated without the use of specialized equipment or cleanroom procedures. A schematic of the device's layers and an assembled cross-section are shown in Figure 1. The top layer of the device was a 0.063-inch (1.6 mm) thickness sheet of 5052 aluminum perforated with an array of 0.125-in. (3.2 mm) diameter holes (McMaster-Carr item no. 5250N37); all holes and arrays in other layers of the device were patterned to align with the aluminum sheet's perforations. The aluminum sheet served as the opposing electrode to the CNF mats. A glass slide with an indium tin oxide (ITO) coating (8–12 Ω, SPI Supplies) was the bottom layer of the device.

The 4 mm diameter CNF mat disks were arrayed atop the ITO such that a single electrical connection to the ITO also connected to every CNF mat disk in parallel. Two separate layers of double-sided adhesive (DSA) were layered between the aluminum sheet and the ITO slide with mat array. Both DSA layers were patterned with an array of holes using a cutter plotter (Roland CAMM-1 GS-24). The first layer had a thickness of 49 μm (Adhesives Research ARcare 92712) and hole diameters of 5 mm. This size allowed the CNF mat disks to lie within the holes of this layer. The second DSA layer was 142 μm thick (Adhesives Research ARcare 90880) and patterned with holes 3 mm in diameter. This layer ensured uniform electrode separation between the CNF mats and the aluminum sheet; it also compressed the CNF mat disks' edges to ensure a uniform electrical connection to the underlying ITO. Adhesive copper tape was used to aid in connecting the device's electrodes to electrical equipment.

In practice, the fabrication process was performed starting with the aluminum sheet, then aligning and applying the remaining layers on the underside of the aluminum and ending with the ITO slide. The device's construction allowed liquid samples to be added and removed from the wells without altering the electrode arrangement or electrical connections. Each device was fabricated with between 18 and 24 wells, which could be used individually for testing with various electric field parameters.

3.1.3 | Sample preparation

The tested sample was a suspension of 1.0 μm red fluorescent polystyrene microspheres (Fluoro-Max, initially 1% solids). The sample was prepared by adding two drops (approximately 20 μL) of the packaged particle suspension and 0.1% Tween 20 (Thermo Scientific) to 5 mL of DI water (filtered from Milli-Q ultrapure water system). The final particle suspension had a measured electrical conductivity of 3.08 mS/m (Denver Instrument Model 220 meter). This suspension as prepared contained approximately 76 000 particles per microliter. The bulk conductivity of polystyrene microspheres was negligible compared to the effect of the surface conductance, which was taken as $K_s = 2.34 \pm 0.33$ nS for medium conductivity between 2 and 10 mS/m as found by Vahey and Voldman for red carboxylate-modified polystyrene microspheres [23]. By Equation (2), this results in a calculated total particle conductivity of 9.36 mS/m. The assumed relative permittivities of the medium and particles were $\varepsilon_{r,m} = 78.5$ and $\varepsilon_{r,p} = 2.6$, respectively [24].

15222683, 0, Downloaded from https://analyticalsciencejournals.onlinelibrary.wiley.com/doi/10.1002/elps.202400051 by University Of Louisville, Wiley Online Library on [11/11/2024]. See the Terms and Conditions (https://onlinelibrary.wiley.com/terms-and-conditions) on Wiley Online Library for rules of use; OA articles are governed by the applicable Creative Commons License

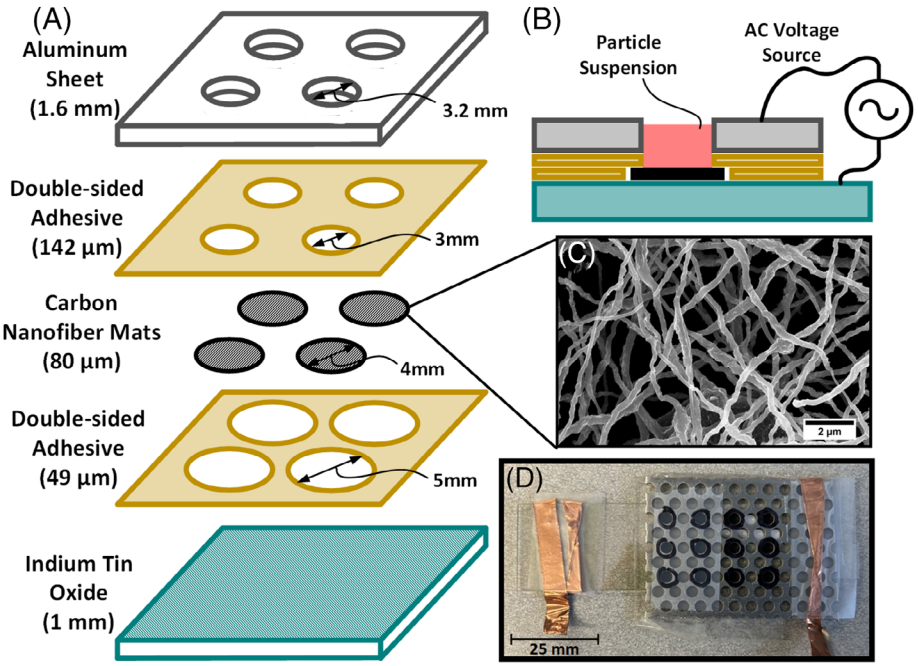

FIGURE 1 (A and B) Exploded view and cross-section view, respectively, of the well-based device schematic used for dielectrophoretic particle trapping. (C) A scanning electron microscopy (SEM) image of the conductive carbon nanofiber (CNF) mat. (D) An image from the top side of one of the assembled devices.

3.2 | Experimental methods

3.2.1 | Electrical components

A Keithley 3390 waveform generator was used to supply an AC voltage between the electrodes. The signal from the waveform generator was passed through a Trek 2100HF amplifier. The signal was passed through capacitors both before (3.3 nF) and after (10 nF) the amplifier to act as high-pass filters and remove DC leakage from the electrical signal. An Agilent 34405A digital multimeter was used to measure the signal amplitude and frequency as delivered to the electrodes after being passed through the amplifier and capacitors. Due to the frequency-dependent nature of the capacitors and amplifier, particularly at larger frequencies, the waveform generator voltage amplitude was adjusted until the as-delivered signal measured 20 V_{rms}. These measurements were made at the device itself so that any affect by the capacitors on the amplitude of the signal originating from the waveform generator would not be relevant.

3.2.2 | Testing procedure

Tests were performed with liquid in only one well at a time so that the sequence of applied voltages and AC frequencies could be randomized for repeated experiments. Liquids were added to the wells using a micropipette. Initially, 10 µL of DI water with 0.1% Tween 20 was added to presoak the CNF mat. With the DI water added, the device was placed under vacuum in a desiccator for 5 min to evacuate any air pockets within or around the CNF mat. Following this, 4 µL of the microsphere suspension was pipetted into the well. The combined liquid medium in the well during experiments therefore contained approximately 22 000 particles/µL. An AC potential was applied between the ITO and aluminum sheet for 5 min, at which time the waveform generator output was disabled. Then the fluid, as well as the remaining suspended microspheres, was removed from the well by inserting a cotton swab into the well for approximately 5 s.

AC frequencies of 30, 100, 300, 600, and 1 MHz were applied with a potential of 20 V_{rms} across the electrodes. Control tests involved the same procedure, excluding the application of an electric field. Tests were repeated with each combination of electric field parameters on six wells, which were divided evenly among the well devices at randomly determined wells among each device's array to avoid any bias related to the well location or variation between the fabrication of different devices.

3.2.3 | Data collection and analysis

The wells were allowed to dry completely before being photographed. A Nikon Eclipse Ti inverted fluorescent

15222683, 0, Downloaded from https://analyticalsciencejournals.onlinelibrary.wiley.com/doi/10.1002/elps.202400051 by University Of Louisville, Wiley Online Library on [11/11/2024]. See the Terms and Conditions (https://onlinelibrary.wiley.com/terms-and-conditions) on Wiley Online Library for rules of use; OA articles are governed by the applicable Creative Commons License

microscope with a 3× total magnification was used with an XCite 120 for illumination. The white light illumination was passed through a DsRed filter cube to view the fluorescent microspheres trapped by the CNF mat. The wells were photographed using a Canon Eos Rebel T7i (6000 × 4000, 3.72 μm/pixel) digital camera using ISO 6400 and 1/5 s shutter speed.

A MATLAB image analysis script was used to process the data from the digital images. Each image was converted to grayscale, and a circle was fitted to the perimeter of the well based on five user-selected points on the well's edge. The image was then cropped to include only pixels inside the circle. From there, each pixel was assigned the binary value 0 or 1 if its lightness was below or above, respectively, a threshold of 0.15. Pixel islands smaller than 20 pixels in size were removed from consideration, and then each remaining white pixel was counted. The pixel count of each image was used as the metric for the comparison of particle trapping with different electric field parameters. To avoid noise in the data associated with particles stuck to the sharp edge of the aluminum sheet, white pixels from the outer 20% of the circle (by area) were excluded from the final pixel counts. Chauvenet's criterion was then applied to remove statistical outliers from each group [25]. Refer to Figure S5 for representative images from each step of the MATLAB analysis.

4 | RESULTS AND DISCUSSION

4.1 | Expected behavior

The electric field frequencies for these experiments were chosen to span a range of Re[CM] values. At the low frequencies (30 and 100 kHz), the magnitude of the DEP force was near its greatest intensity. Conversely, the higher frequencies (600 kHz and 1 MHz) were selected to exhibit lower DEP strength. Figure 2 shows Re[CM] plotted against AC frequency using the referenced and measured dielectric properties of the media and materials for this study.

The intensity of other EHD phenomena (ET flow, ACEO) was also known to decay with increasing field frequency. Based on the expectation that all EHD phenomena contributed positively to particle trapping, it was assumed that the number of trapped particles would decrease as AC frequency increased. As all test frequencies were within the range in which Re[CM] > 0, it was expected that all test groups would effectively trap particles to some degree, whereas the control group with no applied electric field would show comparatively low numbers of particles.

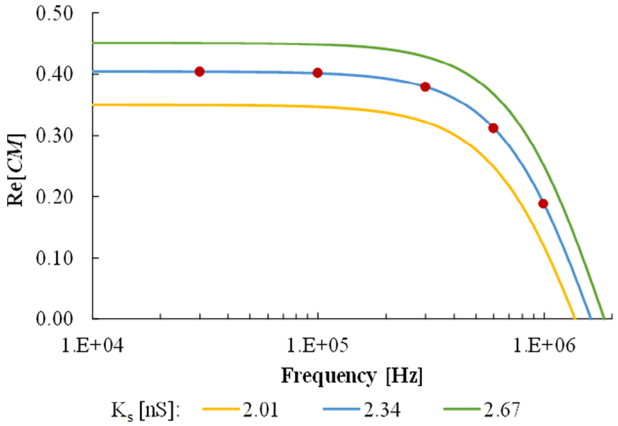

FIGURE 2 Plot of Re[CM] versus AC field frequency for fluorescent microspheres of conductivity 9.36 mS/m and relative permittivity 2.6 within medium with conductivity 3.08 mS/m and relative permittivity 78.5. Multiple curves are plotted corresponding to the relevant uncertainty of particle surface conductance values (2.34 ± 0.33 nS). Red markers indicate electric field frequencies used in experiments.

4.2 | Results

Images of one well from each experimental group are shown in Figure 3A–F. The images chosen to represent each group were those in which the trapped particle pixel count (excluding the outer 20% of the well by area as illustrated by Figure 3G) was nearest to the mean for their respective group. Figure 3H shows a graph of average counted pixels among wells in each experimental group. The greatest numbers of trapped particles appeared near the perimeters of the wells where electric field strength was greatest. Furthermore, with data from the entirety of the well images included in the analyses, all test groups showed trapped particles in significantly greater quantities than the control group in which no electric field was applied. The particles trapped in the control group CNF mats were likely due to diffusion, sedimentation, and/or electrostatic attraction. These observations were consistent with expectations.

By contrast, it can be seen from both parts D and H of Figure 3 that the most significant particle trapping occurred at 600 kHz, which was notably inconsistent with expectations. It was noted that for the data, including only pixels within the inner 80% of the wells by area, the 600 kHz group was the only group in which a significantly greater number of particles were trapped than in the control group. Therefore, it was apparent that across the interior region of the CNF mat where electric field strength was weakest, DEP trapping was insignificant at all other field frequencies. This was a notable result that warranted a further investigation of the relevant

15222683, 0, Downloaded from https://analyticalsciencejournals.onlinelibrary.wiley.com/doi/10.1002/elps.202400051 by University Of Louisville, Wiley Online Library on [11/11/2024]. See the Terms and Conditions (https://onlinelibrary.wiley.com/terms-and-conditions) on Wiley Online Library for rules of use; OA articles are governed by the applicable Creative Commons License

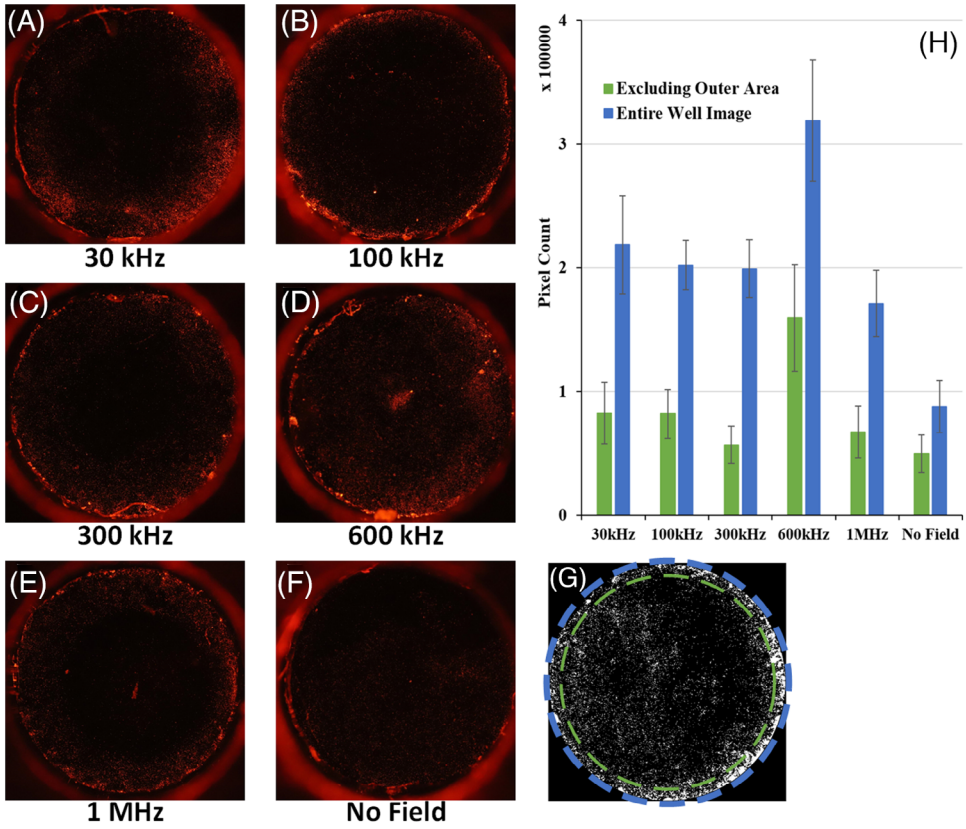

FIGURE 3 (A–F) Representative images of microfluidic wells showing fluorescent microspheres trapped using a range of electric field frequencies with an applied potential of 20 V_{rms}. Images were chosen such that the trapped particle pixel count was nearest to the respective group average. (G) Example of a well image after processing with dashed circles indicating the regions of data represented by the bar graph. The image shown is from a trial conducted at 600 kHz. (H) Average counted pixels for well images in each test frequency group after outliers removed. Data are shown for counts of the entire well image as well as counts excluding the outer 20% of the well by area. Error bars show standard error ($\sigma/\sqrt{n}$).

EHD phenomena. Theoretical calculations involving the frequency-dependent magnitudes of ET hydrodynamics and ACEO were performed to determine whether either phenomenon might have contributed significantly to particle trapping performance, either positively or negatively (see the Supporting Information section). It was determined from this analysis that ACEO was negligible for all tested frequencies, whereas the magnitude of ET flow varied significantly across the test frequency range as did that of DEP. It was noted that at 600 kHz, the theoretical ET flow velocity was reduced somewhat more significantly than the DEP force (Figure S2). At the lower test frequencies (30, 100, and 300 kHz), ET flow was at or near its theoretical maximum in magnitude; at higher frequencies, such as the test frequency of 1 MHz, both ET flow and the DEP force were significantly weakened. Based on this theoretical analysis, it was hypothesized that the unexpected results of the experimental study could be explained by a positive contribution to particle trapping by DEP balancing against a net negative contribution to trapping by ET flow. Because both DEP and ET flows are functions of fluid medium conductivity σ_m, subsequent tests were performed using a particle suspension with lower electrical conductivity to evaluate this hypothesis. A further discussion of these theoretical calculations using theoretical relations and referenced properties from Refs. [22, 26, 27] can be found in the Supporting Information section.

4.3 | Subsequent experiments

4.3.1 | Lower conductivity testing

For the additional trials, another well-based device was fabricated using the same processes previously employed. CNF mat trapping experiments were performed using identical testing procedure and equipment with a subset of the original test frequencies (100, 300, and 600 kHz). The only nominal difference between the original and new

15222683, 0, Downloaded from https://analyticalsciencejournals.onlinelibrary.wiley.com/doi/10.1002/elps.202400051 by University Of Louisville, Wiley Online Library on [11/11/2024]. See the Terms and Conditions (https://onlinelibrary.wiley.com/terms-and-conditions) on Wiley Online Library for rules of use; OA articles are governed by the applicable Creative Commons License

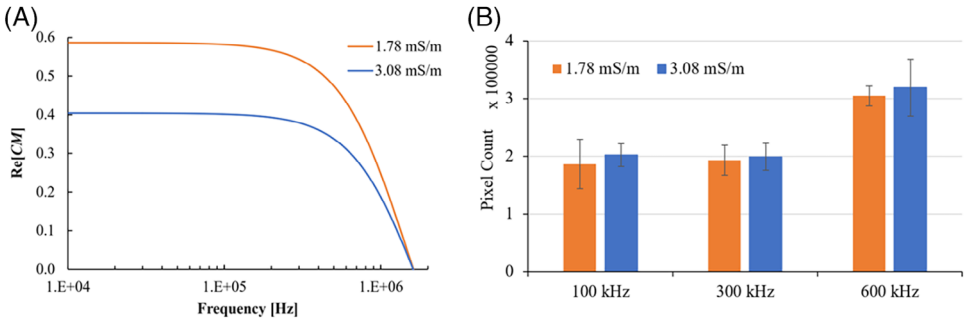

FIGURE 4 (A) Re[CM] plotted against electric field frequency across the relevant range of test frequencies for both fluid medium conductivities. Note that the blue curve is identical to that shown in Figure 2. (B) Average counted pixels for well images in each common test frequency group for both fluid conductivities after outliers removed. Data are shown for counts of the entire well image only. Error bars show standard error ($\sigma/\sqrt{n}$).

experiments was the conductivity of the fluid medium. Although the previous tests were performed at fluid conductivity of 3.08 mS/m, a new particle suspension and DI + Tween pre-wetting solution were prepared with conductivity 1.78 mS/m. This lower conductivity was achieved by reducing the amount of Tween-20 in the solution. This change did not result in any observable particle agglomeration and/or settling on the timescale of the experimental trials. Fluorescent PS microspheres (1.0 μm) were added to the same concentration as that of the previous particle suspension.

It can be seen from Equation (4) that decreasing fluid conductivity would result in a reduction of the ET flow velocity, whereas Equation (1) shows that the DEP force would increase in magnitude. A comparison of Re[*CM*] plotted against frequency for both tested fluid conductivities is shown in Figure 4A. At this point, it was believed that ET flow might contribute negatively to particle trapping. Therefore, the expected result of these tests was an increase in particle trapping at all frequencies relative to the original results as shown in Figure 3H. Figures S2 and S3 show normalized magnitudes of DEP and ET flow plotted against frequency for the two fluid conductivities used in this study. The curves plotted in those figures justify the expectation of increased trapping at lower fluid conductivity based on the assumption that ET flow reduces trapping performance. Six repetitions at each frequency were performed, and identical imaging and analysis steps were performed to quantify particle trapping as those used previously. The particle trapping performance is compared between conductivities in Figure 4B.

Figure 4B shows the quantified particle trapping metric is not significantly different between the two conductivity cases at any of the three common test frequencies. This was contrary to the expected results. The apparent lack of sensitivity to fluid conductivity indicated that other factors (such as a variation in electric field strength with frequency) were affecting the particle trapping results more significantly than would the theoretical changes in DEP strength and ET flow velocity. This led to subsequent investigation to determine the impedance spectrum of the assembled well-based device.

4.3.2 | Impedance spectroscopy

An HP4294A Precision Impedance Analyzer was used to measure the impedance spectra of the well based device. The measurements determined the average of three (3) passes across a range of frequencies, which included the relevant range used in particle trapping experiments. Measurements were taken for a "dry" device (no fluid was contained within any of the wells) and for the same device with one "wet" well containing 14 μL of the 1.78 mS/m DI + Tween solution. The resulting impedance spectra are shown in Figure 5.

Figure 5 shows the impedance spectra for the "dry" and "wet" well device between 1 kHz and 10 MHz. As shown from the "dry" device spectrum, the device overall acts as a capacitor likely due to the relatively large surface area intact of the DSA. With one well containing liquid, the impedance varies less significantly for AC frequencies less than 100 kHz, but this impedance spectrum also shows an inverse proportionality between frequency and impedance at frequencies greater than 100 kHz. Therefore, at the level of the entire test device, the apparatus behaves as a capacitor for frequencies ≥100 kHz. For both the wet and dry impedance spectra, the device-level impedance decreased approximately threefold between 100 and 300 kHz and again equally divided between 300 and 600 kHz. Refer to Figure S4 for a simplified equivalent circuit model of the "dry" and "wet" device.

15222683, 0, Downloaded from https://analyticalsciencejournals.onlinelibrary.wiley.com/doi/10.1002/elps.20240005 by University Of Louisville, Wiley Online Library on [11/11/2024]. See the Terms and Conditions (https://onlinelibrary.wiley.com/terms-and-conditions) on Wiley Online Library for rules of use; OA articles are governed by the applicable Creative Commons License

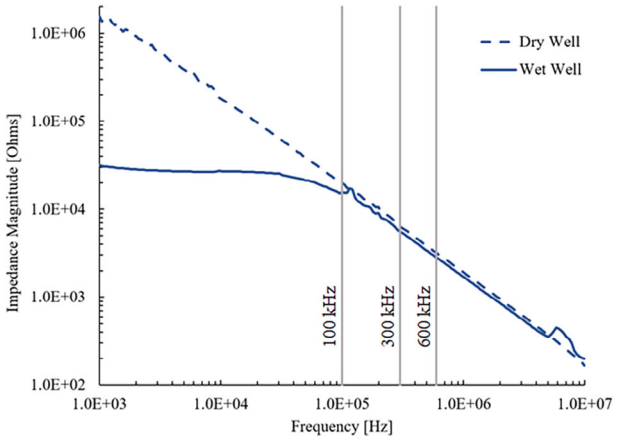

FIGURE 5 Measured impedance spectra of a well-based conductive carbon nanofiber (CNF) mat testing device plotted log–log against frequency when dry and with one well containing 14 μL of a 1.78 mS/m DI + Tween solution, with repeated test frequencies 100, 300, and 600 kHz, denoted by vertical lines.

For the wet device, as frequency increased past 100 kHz, the overall device impedance decreased, which will increase current density, thereby increasing the electric field within the well and increasing the DEP force on the suspended microparticles. The relative increase in particle trapping at 600 kHz relative to the other test frequencies is also explained by this result. For frequencies lower than 600 kHz, the electric field, and even more so the DEP force, were significantly weakened. At 1 MHz, although the electric field strength was greater than that at 600 kHz, with impedance decreasing by ~1.7× over this range, the reduction in Re[*CM*] over the same range results in a net reduction in particle trapping.

5 | CONCLUDING REMARKS

The results of the well-based CNF mat device showed electric field frequency dependence in electrokinetic polystyrene microsphere trapping performance. Both the frequency dependence of DEP and the system-level dielectric behavior were shown to affect particle trapping. The results of this study provide insight for the design of future electrokinetic systems utilizing CNF mats for particle trapping. The simplicity of the current well-based design platform could be adapted for use in future systems; consideration of the capacitive behavior of such devices, which seems to be a dominant factor contributing to overall trapping performance, would enable the informed selection of electric field parameters for specific particle trapping applications. The capacitive behavior may also be reduced, if desired, by decreasing the overall system footprint (i.e., reducing the number, size, and/or spacing of wells). Future experimental and numerical investigations could provide further insight regarding the interaction between the frequency dependence of both relevant electrokinetic phenomena and system-level impedance. A better understanding of such interactions would assist design decisions for throughput-based electrokinetic particle trapping systems utilizing CNF mats.

ACKNOWLEDGMENTS

This research work was supported by National Science Foundation under award no. 2121008. We would also like to thank the engineers in the Micro/Nano Technology Center at the University of Louisville for the sample-specific direction for imaging under the electron microscope.

CONFLICT OF INTEREST STATEMENT

The authors have declared no conflicts of interest.

DATA AVAILABILITY STATEMENT

The data that support the findings of this study are available from the corresponding author upon reasonable request.

ORCID

J. Hunter West https://orcid.org/0000-0003-0882-9406
Stuart J. Williams https://orcid.org/0000-0002-1678-7544

REFERENCES

1. Li M, Anand RK. Cellular dielectrophoresis coupled with single-cell analysis. Anal Bioanal Chem. 2018;410:2499–515.
2. Abd Rahman N, Ibrahim F, Yafouz B. Dielectrophoresis for biomedical sciences applications: a review. Sensors. 2017;17:449.
3. Pesch GR, Du F. A review of dielectrophoretic separation and classification of non-biological particles. Electrophoresis. 2021;42:134–52.
4. Pethig R. Review article—dielectrophoresis: status of the theory, technology, and applications. Biomicrofluidics. 2010;4:022811.
5. Wood NR, Wolsiefer AI, Cohn RW, Williams SJ. Dielectrophoretic trapping of nanoparticles with an electrokinetic nanoprobe. Electrophoresis. 2013;34:1922–30.
6. Barik A, Chen XS, Oh SH. Ultralow-power electronic trapping of nanoparticles with sub-10 nm gold nanogap electrodes. Nano Lett. 2016;16:6317–24.
7. Sabuncu AC, Liu JA, Beebe SJ, Beskok A. Dielectrophoretic separation of mouse melanoma clones. Biomicrofluidics. 2010;4:021101.
8. Farasat M, Chavoshi SM, Bakhshi A, Valipour A, Badieirostami M. A dielectrophoresis-based microfluidic chip for trapping circulating tumor cells using a porous membrane. J.Micromech.Microeng. 2022;32:015008.
9. Cho YK, Kim S, Lee K, Park C, Lee JG, Ko C. Bacteria concentration using a membrane type insulator-based dielectrophoresis in a plastic chip. Electrophoresis. 2009;30:3153–59.
10. Lee HJ, Yasukawa T, Suzuki M, Taki Y, Tanaka A, Kameyama M, et al. Rapid fabrication of nanoparticles array on polycarbonate

15222683, 0, Downloaded from https://analyticalsciencejournals.onlinelibrary.wiley.com/doi/10.1002/elps.20240005 by University Of Louisville, Wiley Online Library on [11/11/2024]. See the Terms and Conditions (https://onlinelibrary.wiley.com/terms-and-conditions) on Wiley Online Library for rules of use; OA articles are governed by the applicable Creative Commons License

membrane based on positive dielectrophoresis. Sens Actuators B Chem. 2008;131:424–31.
11. Sandison ME, Cooper JM. Nanofabrication of electrode arrays by electron-beam and nanoimprint lithographies. Lab on a Chip. 2006;6:1020–25.
12. Madiyar FR, Syed LU, Culbertson CT, Li J. Manipulation of bacteriophages with dielectrophoresis on carbon nanofiber nanoelectrode arrays. Electrophoresis. 2013;34:1123–30.
13. Salafi T, Zeming KK, Zhang Y. Advancements in microfluidics for nanoparticle separation. Lab on a Chip. 2017;17:11–33.
14. Pesch GR, Lorenz M, Sachdev S, Salameh S, Du F, Baune M, et al. Bridging the scales in high-throughput dielectrophoretic (bio-) particle separation in porous media. Sci Rep. 2018;8:10480.
15. Lorenz M, Malangré D, Du F, Baune M, Thöming J, Pesch GR. High-throughput dielectrophoretic filtration of sub-micron and micro particles in macroscopic porous materials. Anal Bioanal Chem. 2020;412:3903–14.
16. Mondal TK, West JH, Williams SJ. An electrospun nanofiber mat as an electrode for AC-dielectrophoretic trapping of nanoparticles. Nanoscale. 2023;15:18241–49.
17. Pohl HA. The motion and precipitation of suspensoids in divergent electric fields. J Appl Phys. 1951;22:869–71.
18. Castellanos A, Ramos A, González A, Green NG, Morgan H. Electrohydrodynamics and dielectrophoresis in microsystems: scaling laws. J Phys D Appl Phys. 2003;36:2584–97.
19. Ramos A, Morgan H, Green NG, Castellanos A. AC electric-field-induced fluid flow in microelectrodes. J Colloid Interface Sci. 1999;217:420–22.
20. Mishchuk NA, Heldal T, Volden T, Auerswald J, Knapp H. Micropump based on electroosmosis of the second kind. Electrophoresis. 2009;30:3499–506.
21. Hossan MR, Dutta D, Islam N, Dutta P. Review: electric field driven pumping in microfluidic device. Electrophoresis. 2018;39:702–31.
22. Ramos A, (Ed.). Electrokinetics and electrohydrodynamics in microsystems. CISM Courses and Lectures, Vol. 530, Springer Science+Business Media, 2011.
23. Vahey MD, Voldman J. High-throughput cell and particle characterization using isodielectric separation. Anal Chem. 2009;81:2446–55.
24. White CM, Holland LA, Famouri P. Application of capillary electrophoresis to predict crossover frequency of polystyrene particles in dielectrophoresis. Electrophoresis. 2010;31:2664–2671.
25. Tavoularis S. Measurement in fluid mechanics. Cambridge: Cambridge University Press; 2005.
26. González A, Ramos A, Morgan H, Green NG, Castellanos A. Electrothermal flows generated by alternating and rotating electric fields in microsystems. J Fluid Mech. 2006;564:415–33.
27. Molahalli V, Chaithrashree K, Singh MK, Agrawal M, Krishnan SG, Hegde G. Past decade of supercapacitor research—lessons learned for future innovations. J Energy Storage. 2023;70:108062.

SUPPORTING INFORMATION

Additional supporting information can be found online in the Supporting Information section at the end of this article.

How to cite this article: West JH, Mondal TK, Williams SJ. Electrokinetic particle trapping in microfluidic wells using conductive nanofiber mats. Electrophoresis. 2024;1–9. https://doi.org/10.1002/elps.202400051

15222683, 0, Downloaded from https://analyticalsciencejournals.onlinelibrary.wiley.com/doi/10.1002/elps.202400051 by University Of Louisville, Wiley Online Library on [11/11/2024]. See the Terms and Conditions (https://onlinelibrary.wiley.com/terms-and-conditions) on Wiley Online Library for rules of use; OA articles are governed by the applicable Creative Commons License